Local metallic and structural properties of the strongly correlated metal $LaNiO_3$ using ^{8}Li β-NMR

Victoria L. Karner,[1,2,*] Aris Chatzichristos,[2,3] David L. Cortie,[1,2,3,†] Martin H. Dehn,[2,3] Oleksandr Foyevtsov,[2,3] Kateryna Foyevtsova,[2,3] Derek Fujimoto,[2,3] Robert F. Kiefl,[2,3,4] C. D. Philip Levy,[4] Ruohong Li,[4] Ryan M. L. McFadden,[1,2] Gerald D. Morris,[4] Matthew R. Pearson,[4] Monika Stachura,[4] John O. Ticknor,[1,2] Georg Cristiani,[5] Gennady Logvenov,[5] Friederike Wrobel,[5] Bernhard Keimer,[5] Junjie Zhang,[6,‡] John F. Mitchell,[6] and W. Andrew MacFarlane[1,2,4,§]

[1]*Department of Chemistry, University of British Columbia, Vancouver, British Columbia V6T 1Z1, Canada*

[2]*Stewart Blusson Quantum Matter Institute, University of British Columbia, Vancouver, British Columbia V6T 1Z4, Canada*

[3]*Department of Physics and Astronomy, University of British Columbia, Vancouver, British Columbia V6T 1Z1, Canada*

[4]*TRIUMF, 4004 Wesbrook Mall, Vancouver, British Columbia V6T 2A3, Canada*

[5]*Max Planck Institute for Solid State Research, 70569 Stuttgart, Germany*

[6]*Materials Science Division, Argonne National Laboratory, Argonne, Illinois 60439, United States of America*

(Received 18 June 2019; published 7 October 2019; corrected 28 February 2020)

We report β-detected NMR of ion-implanted ^{8}Li in a single crystal and thin film of the strongly correlated metal $LaNiO_3$. Spin-lattice relaxation measurements reveal two distinct local environments, both metallic as evident from T-linear Korringa $1/T_1$ below 200 K with slopes comparable to other metals. A small approximately temperature-independent Knight shift of $\sim$74 ppm is observed, yielding a normalized Korringa product characteristic of substantial antiferromagnetic correlations. We find no evidence for a magnetic transition from 4 to 310 K. The similarity of these features in the two very different samples indicates that they are intrinsic and unrelated to dilute oxygen vacancies. We attribute the two environments to two distinct but similar crystallographic ^{8}Li sites and not to any form of phase inhomogeneity, but this is inconsistent with the conventional rhombohedral structure of $LaNiO_3$, and also cannot be simply explained by the common alternative orthorhombic or monoclinic distortions.

DOI: 10.1103/PhysRevB.100.165109

I. INTRODUCTION

On the path to understanding and controlling correlated electrons in solids, a great deal of effort has gone into studying how the Fermi liquid state can be destabilized to yield other more exotic ground states below a metal-insulator transition (MIT) [1]. The rare-earth (R) perovskite nickelates $RNiO_3$ are a unique and important example that remains challenging despite intense scrutiny [2–5]. Besides the MIT, further interest in $RNiO_3$ stems from their close relation to the high-T_c cuprates, both as potential superconductors [6,7] and for what the absence of nickelate superconductivity reveals about the cuprates. Among the $RNiO_3$ series, $LaNiO_3$ (LNO) is unique in avoiding the MIT, remaining a paramagnetic metal to low temperature, making it particularly interesting and potentially useful. Though metallic, $LaNiO_3$ is highly correlated [8,9], with a strongly enhanced magnetic response [10] and electronic heat capacity [8]. The origin of these properties and even the persistence of the metallic state itself remain open questions [11,12].

Recently, epitaxial strain and dimensional confinement have been used to modify the properties of $RNiO_3$ [5,13], including causing an MIT in $LaNiO_3$ [14]. Advances in high-pressure O_2 crystal growth have also made high-quality single crystals of $LaNiO_3$ available for the first time [15–17], opening the prospect for refined studies of the bulk. Surprisingly, recent results on one crystal have cast doubt on LNO's characterization as a nonmagnetic metal, instead concluding that, in sufficiently pure stoichiometric form, it is magnetically ordered below $T_N \approx 157$ K [16]. Other crystals show the propensity for slight substoichiometry and the ordering of oxygen vacancies into defect phases that may explain the observed magnetism [17,18].

Here we report results from β-detected NMR (β-NMR) measurements of implanted highly polarized $^8Li^+$ ions in two very different samples of LNO—a high-quality single crystal and an epitaxial thin film. Like muon spin rotation (μSR) [19], β-NMR provides a sensitive local magnetic probe of solids, but, in contrast, due to the much longer lifetime, it is sensitive to the metallic state in close analogy with conventional NMR [20]. Using a low-energy beam of implanted nuclei, β-NMR has the additional capability that it can easily be applied to thin films [21]. In both samples, we find clear indication of conventional Korringa spin-lattice relaxation (SLR) below 200 K, with no evidence of a magnetic transition from 4 to 310 K. We find two distinct, equally abundant, metallic local

*vkarner@chem.ubc.ca

†Present address: Institute for Superconducting and Electronic Materials, Australian Institute for Innovative Materials, University of Wollongong, North Wollongong, New South Wales 2500, Australia.

‡Present address: Materials Science and Technology Division, Oak Ridge National Laboratory, Oak Ridge, Tennessee 37830, United States of America.

§wam@chem.ubc.ca

environments for the implanted probe that we attribute to two similar but distinct crystallographic sites for $^8Li^+$ in the lattice. The quantitative similarity between the two samples strongly suggests all of these features are intrinsic.

II. EXPERIMENTAL

In β-NMR, highly spin-polarized β-radioactive ions are implanted into the sample, and the NMR is detected by the subsequent β decay. The β-decay asymmetry is proportional to the average longitudinal spin polarization, with a proportionality constant A_0 that depends on the detection geometry and properties of the decay [22]. The asymmetry is measured by combining β count rates from two opposing scintillation detectors. All of the experiments were conducted using the β-NMR spectrometer at TRIUMF in Vancouver, Canada [22,23]. The $^8Li^+$ probe nuclei (spin $I = 2$, gyromagnetic ratio $\gamma/2\pi = 6.3016$ MHzT^{-1}, electric quadrupole moment $Q = +32.6$ mb, and radioactive lifetime $\tau = 1.21$ s) were spin-polarized in-flight using optical pumping [24] and subsequently ion-implanted into the LNO samples. The implantation energies were 2.9 keV and 27.9 keV corresponding to mean depths of 12.9 nm and 99.5 nm (details in Appendix A).

In an applied magnetic field $B_0 = 6.55$ T provided by a high-homogeneity superconducting solenoid in persistence mode, two types of measurements were performed: Relaxation and resonance. With a pulsed $^8Li^+$ beam, SLR data were collected by monitoring the depolarization during and after the 4 second long pulse. During the pulse, the polarization approaches a dynamic steady-state value, while afterward, it relaxes to $\approx$0. Since the probe nucleus is polarized prior to implantation, unlike conventional NMR, no radio frequency (RF) field is required to measure SLR. Resonance measurements used a continuous beam of $^8Li^+$ with a transverse RF field H_1 stepped slowly in frequency through the ^{8}Li Larmor frequency $\nu_0 = \gamma B_0/(2\pi) \approx 41.27$ MHz. On resonance, the ^{8}Li spin precesses rapidly due to the RF field, resulting in a loss of the time-averaged asymmetry. The resonance frequency was calibrated against a single crystal of MgO at 300 K [25].

The film sample was deposited on a single crystal $[LaAlO_3]_{0.3}[Sr_2AlTaO_6]_{0.7}$ (LSAT) substrate by pulsed laser deposition (PLD) and annealed in an O_2-rich environment as described in Ref. [14]. Its thickness was determined by x-ray reflectivity to be 38(1) nm. The LSAT substrate is lattice matched to LNO, minimizing epitaxial strain. The LNO crystal was grown as detailed in Ref. [15]. A 1.5 mm thick slice perpendicular to the pseudocubic [100] direction was cut from a cylindrical boule $\sim$5 mm in diameter. The surface was prepared by polishing with Al_2O_3 suspensions until a mirror-like surface was obtained. The samples were affixed to polished sapphire plates attached to a He cold-finger cryostat.

Although the crystals have a rather low average O deficiency (determined by thermogravimetric analysis to be $\sim$0.015/formula unit), it is possible that this could influence the measured properties. Indeed, large O vacancy concentrations can be purposely generated in $LaNiO_3$ with the appearance of supercell defect phases that order magnetically, with composition $LaNiO_{2.75}$ and $LaNiO_{2.5}$ [18]. If the O vacancy phases are uniformly distributed, they would amount to <5 mol %; however, in the case of nonuniform distribution, the concentration of ordered superlative phases would be sample dependent and could exceed this upper bound.

III. RESULTS AND ANALYSIS

A. Spin-lattice relaxation

Representative SLR data are shown in Fig. 1. At low temperatures in both the crystal and film, the relaxation is slowest, with the rate increasing monotonically with temperature. We identify a small-amplitude fast-relaxing component at early times as a background signal due to ^{8}Li stopping outside the sample. It is easily distinguished from the sample signal with a nearly temperature-independent rate faster than the sample at all temperatures. The remaining signal from LNO is also not comprised of a single relaxing component, but has two distinct SLR contributions with different rates. With this in mind, we require a model relaxation function $R(t)$, the analog of the magnetization recovery curve in NMR, to fit the data. The simplest form providing a good fit is a triexponential, which encapsulates the biexponential signal from LNO, as well as the background. Specifically, at time t after an ^{8}Li arriving at time t',

$$R(t,t') = f_S[(1-f_f)e^{-\lambda_s(t-t')} + f_f e^{-\lambda_f(t-t')}] + (1-f_S)e^{-\lambda_b(t-t')}, \quad (1)$$

where $\lambda_i \equiv 1/T_1^i$ $(i = s, f, b)$ are the SLR rates, $f_f \in [0,1]$ is the fast-relaxing fraction, f_S is the fraction of ^{8}Li in the sample, and the third term is the background. In order to fit the data, a global procedure was used wherein all spectra for each sample (i.e., at every temperature) were fitted simultaneously using a custom C++ code and the MINUIT minimization routines [26] provided by the ROOT framework [27]. Best fits were obtained using temperature-independent fractions: $f_f = 0.50(3)$ for both samples and $f_S = 0.85(6)$ for the crystal and 0.80(6) for the film (see Appendix B), leaving λ_i as the only temperature-dependent parameters. The fit quality is good in each case: $\chi^2 = 0.94$ (crystal) and 1.05 (film).

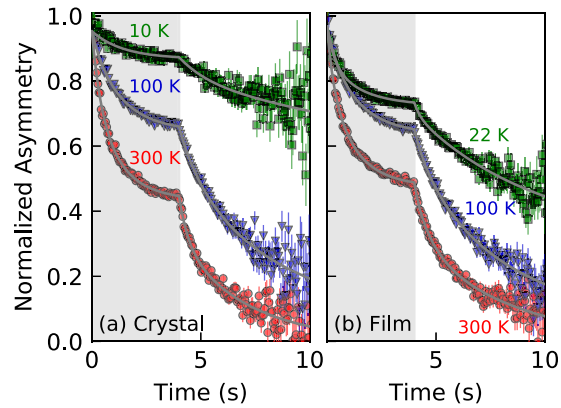

FIG. 1. Examples of SLR data for $^8Li^+$ in $LaNiO_3$ with $B_0 = 6.55$ T with fits (lines) using the triexponential of Eq. (1) convoluted with the 4 s beam pulse indicated by the shaded area. The data are normalized by their apparent $t = 0$ asymmetry; see Appendix B.

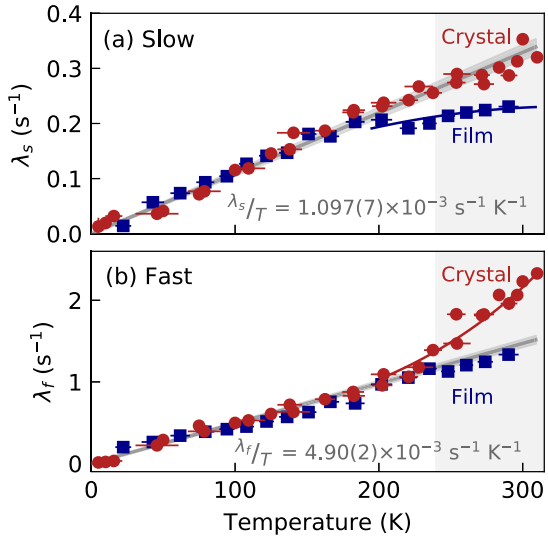

FIG. 2. The slow (a) and fast (b) SLR rates as a function of temperature for ^{8}Li in the $LaNiO_3$ crystal (red circles) and 38 nm film (blue squares). Both rates exhibit a linear Korringa behavior below 200 K that agrees *quantitatively* between the two samples. The thick gray lines are the best-fit slopes, with the values shown. The shading shows the region bounded by a 1σ change to the slope. The vertical shaded region marks the onset of the high-temperature decrease in the single-crystal $\chi_0(T)$ [15] (see text).

The slow and fast SLR rates extracted from the above analysis are shown as a function of temperature in Figs. 2(a) and 2(b). Consistent with the qualitative features in Fig. 1, the

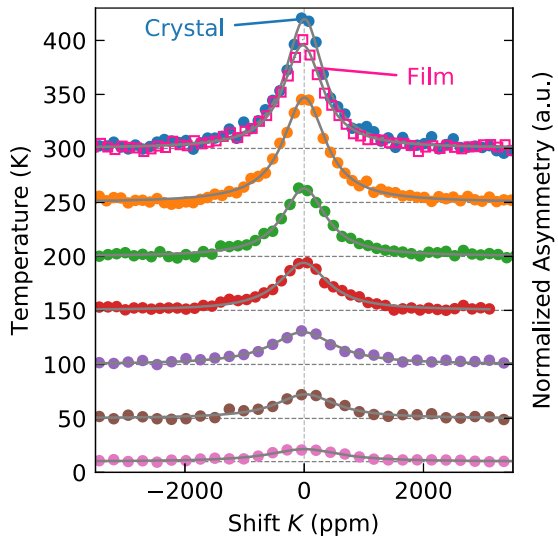

FIG. 3. Temperature dependence of the ^{8}Li resonance in the $LaNiO_3$ crystal at 6.55 T. At low temperature, the resonance is broadest and weakest, with the amplitude growing monotonically and the width narrowing by a factor of ∼2 as the temperature is raised. A small, nearly temperature-independent positive shift relative to MgO is evident. The spectra are normalized by the off-resonance baseline asymmetry and offset to clearly display the temperature dependence. The ^{8}Li resonance in the LNO film at 300 K is also shown (open squares); it is remarkably similar to the crystal both in shift K and width.

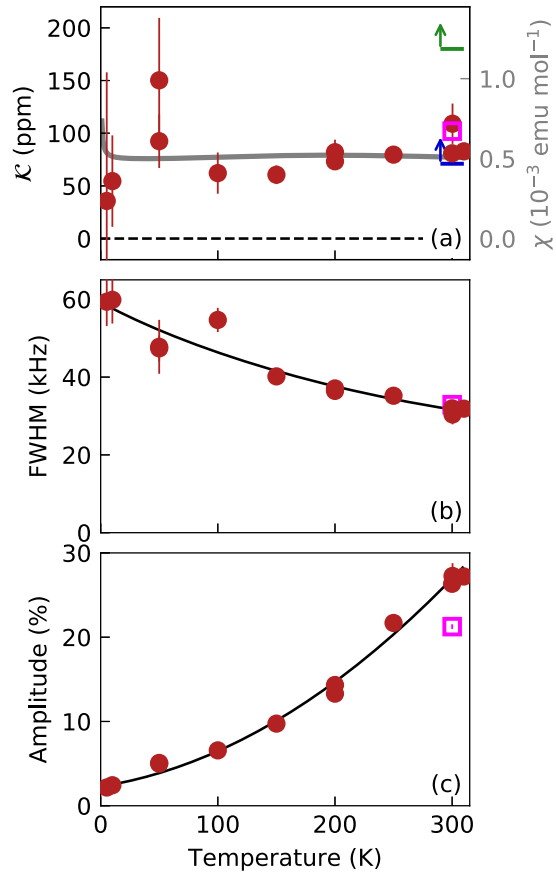

FIG. 4. Temperature dependence of the $^8Li^+$ resonance in the $LaNiO_3$ crystal: (a) Knight shift $\mathcal{K}$, (b) full width at half maximum (FWHM), and (c) amplitude. The amplitude is normalized by the off-resonance baseline asymmetry. In (a), the solid gray curve and right scale show the magnetic susceptibility of the crystal [15]. Horizontal lines show estimates of the Knight shift for the slow (blue) and fast (green) relaxing components at 300 K. The vertical arrows emphasize that the values are lower limits (see text). The black solid curves in panels (b) and (c) are guides. The values for the 38 nm film at 300 K are also shown (open squares).

rates are slowest at the lowest temperature and increase linearly up to ∼200 K, above which there are sample-dependent nonlinearities. Significantly, the fast and slow rates are quantitatively consistent between the two samples, indicating that the behavior is *intrinsic*. Over the linear range ($T < 200$ K), we fit $\lambda_i(T)$ to a line to obtain the slopes in Fig. 2. The two components are present in equal amplitudes in both samples with rates that differ by a factor of ∼4 on average. Their origin is discussed in Sec. IV.

B. Resonances

The resonances (primarily in the crystal) are shown in Fig. 3. In contrast to the multiexponential SLR, the spectrum consists of a single broad line which is narrowest and most intense at the highest temperature. The spectra were fitted to a single Lorentzian, and the resulting parameters are shown in Fig. 4. As the temperature is lowered, the peak broadens by a factor of ∼2, while its amplitude decreases by an order of magnitude. Remarkably, the resonance in the film at 300 K

is comparable to the crystal. Aside from the breadth, the resonance is also slightly positively shifted from the calibration in MgO. We quantify its relative shift by

$$K\,[\mathrm{ppm}] = \left(\frac{\nu_{\mathrm{LNO}} - \nu_{\mathrm{MgO}}}{\nu_{\mathrm{MgO}}}\right) \times 10^6, \tag{2}$$

from which we extract the Knight shift $\mathcal{K}$, due to the conduction band spin susceptibility, after accounting for demagnetization (see Appendix C). The resulting $\mathcal{K} \sim 74$ ppm, independent of temperature, is typical of ^{8}Li in metals but is surprisingly small considering the rather large susceptibility. We discuss the shift further below.

IV. DISCUSSION

Like other atomic solutes, the implanted ^{8}Li nucleus generally has some hyperfine coupling to the conduction band of the host, resulting in a phenomenology very similar to the conventional NMR of metals [20]. The predominant SLR mechanism is usually the Korringa process of spin exchange scattering with the conduction electrons, leading to a characteristic linear dependence of $1/T_1$ on temperature [21]. One distinction from conventional NMR is that the lattice site of the implanted ion is not known *a priori* and is not independently accessible by x-ray diffraction. The site is important because it determines the sensitivity of T_1 to spin fluctuations at finite wave vector, such as when there is some tendency toward antiferromagnetism. The relaxation rate is related to the generalized frequency- and wave-vector-dependent magnetic susceptibility $\chi = \chi' - i\chi''$ via the Moriya expression [28],

$$\frac{1}{T_1} = \frac{4k_B T}{\hbar} \sum_{\vec{q}} \frac{|A(\vec{q})|^2}{(\gamma_e \hbar)^2} \frac{1}{\hbar\omega_0} \chi''(\vec{q}, \omega_0), \tag{3}$$

where the hyperfine form factor $A(\vec{q})$, the spatial Fourier transform of the local hyperfine coupling, acts as a filtering function on the magnetic fluctuations at wave vector $\vec{q}$ and the NMR frequency ω_0. γ_e is the electron gyromagnetic ratio. The resulting site dependence of $1/T_1$ is illustrated by the well-known case of NMR in the cuprates [20].

Another important difference of ^{8}Li β-NMR from, e.g., transition metal NMR is that, as a light isotope, the hyperfine coupling is quite weak, similar to the implanted muon [19], dissolved hydrogen [29], or stable ^{7}Li [30], leading to small Knight shifts on the order of 100 ppm and correspondingly long T_1. The small ^{8}Li shifts make the demagnetization correction particularly important [31]. Unlike the muon [32], the Korringa rate is usually in the accessible window for ^{8}Li: $0.01\tau < T_1 < 100\tau$, making it a useful probe of metals, including correlated oxides such as Sr_2RuO_4 [33].

In the present data, the linearity of $1/T_1$ for both fast and slow components below 200 K (Fig. 2) is clear microscopic evidence of a conventional metallic state, consistent with ^{139}La NMR of bulk powder [34]. Recent powder neutron diffraction suggest that LNO is electronically inhomogeneous, possessing insulating pockets below 200 K [12]. In contrast, we find no evidence for an insulating volume fraction.

β-NMR reports the average behavior over the sampled volume given by the implantation profile (Appendix A) and the millimetric beam spot. An insulating LNO phase would produce another SLR component with amplitude proportional to its volume fraction and a relaxation distinct in both magnitude and temperature dependence. For putative insulating regions, we expect strong local moment magnetism and low-temperature magnetic order. In such regions, the relaxation would be fast and increasing with reduced temperature, peaking at the magnetic freezing, where it might even be so large as to "wipe out" the signal. Based on this, we rule out an insulating magnetic fraction greater than an estimated detection limit of ~5%.

The ^{8}Li resonance spectrum characterizes the static, time-average magnetic properties. Surprisingly, we find a single broad line showing none of the quadrupolar fine structure observed in related insulating perovskites [35–37]. A reduction of the electric field gradient (EFG) compared to isovalent $LaAlO_3$ (LAO) [37] is reasonable in the negative charge transfer picture, as the extra +1 charge of Al^{3+} (vs Ni^{2+}) is spread over the oxide ligands. Metallic screening will further reduce the EFG, evidently resulting in an unresolved splitting of the NMR on the order of the linewidth or less.

The line is, in fact, very broad compared to both other metals and insulating perovskites [35,38]. The temperature dependence of the width [Fig. 4(b)] suggests a combination of a substantial temperature-independent term and one that increases as temperature is decreased. Qualitatively, the former is consistent with quadrupolar broadening due to structural disorder and the latter to magnetic broadening from dilute magnetic defects. However, significantly, the widths in the two samples are comparable at 300 K, the only temperature where we have a resonance in the film. One would not expect extrinsic disorder to be very similar in these vastly different samples, so this agreement is surprising and also points to an intrinsic origin for the width.

To understand these features, we must consider the structural details of perovskites. The nominal rhombohedral structure involves a rotation of the NiO_6 octahedra about any of the equivalent ⟨111⟩ directions of the cubic phase. As a result, the crystal is microtwinned—an intrinsic inhomogeneity that may contribute to the quadrupolar broadening. However, similar microtwinning is also a feature of rhombohedral LAO, where we find large well-resolved quadrupole splitting and substantially smaller linewidth [38], as well as tetragonal $SrTiO_3$ [35]. This suggests twinning alone cannot be responsible for broadening. We return to this point below.

There is also no evidence in the resonance spectra for two environments corresponding to the two relaxing components, but this is not surprising on quantitative grounds, since the observed shift is so small [Fig. 4(a)]. The relaxation rate is determined by the square of the hyperfine coupling [Eq. (3)], while the shift is only linear, so the factor of 4 between the rates implies only a factor of 2 in the shifts, yielding a magnetic splitting on the order of 50 ppm (2 kHz at this B_0, significantly less than the linewidth). Moreover, though the relaxing components are practically equal in their initial (i.e., $t = 0$) asymmetry, the resonance amplitude is determined instead by the time-average asymmetry [39], which, for the fast-relaxing component, is suppressed to at most 27% of the total. Finally, if there is some magnetic broadening, the larger coupling to the fast-relaxing component would likely make its resonance broader and even smaller in relative amplitude.

Based on these considerations, we conclude that the ^{8}Li β-NMR is an unresolved composite of two lines, originating from two distinct local environments, whose spectrum is heavily weighted toward the slow component. The resonance shift (∼74 ppm) is then a weighted average of the two. To illustrate this, we decompose the spectrum at 300 K, assuming equal linewidths and using the relative amplitudes from λ as weights [39], to estimate the Knight shifts of the two components. These are shown in Fig. 4(a), as the horizontal lines for the slow (blue) and fast (green) component where the vertical arrows emphasize that they are lower limits, since the fast-relaxing resonance may be wider (and hence smaller).

From this analysis, we estimate the Knight shift $\mathcal{K} \approx 71(10)$ ppm for the major (slow) component at 300 K. Combining this with the Korringa slope [Fig. 2(a)], we form the normalized Korringa product [20],

$$\mathscr{K} = \frac{T_1 T \mathcal{K}^2}{S} = 0.40(10), \tag{4}$$

where for ^{8}Li, $S = 1.20E - 5$ sK. For an uncorrelated free electron metal, $\mathscr{K} \approx 1$. Our $\mathscr{K}$ is significantly less, indicating substantial antiferromagnetic (AF) correlations [28,40]. The consistency between the two samples is a strong indication that the AF correlations are intrinsic to the bulk of $LaNiO_3$ and unrelated to oxygen vacancies. AF correlations are opposite to a recent Stoner enhancement interpretation of the susceptibility of powder [10] but consistent with the antiferromagnetism of the insulating nickelates [41], including thin layers of LNO [42]. In contrast, ^{139}La NMR finds $\mathscr{K} \approx 1.5$ (i.e., a relaxation rate *slower* than expected from $\mathscr{K} = 1$), suggesting instead ferromagnetic correlations [34].

We now consider potential sources for this substantial discrepancy. One possibility is that, due to the different lattice sites, the different form factors in Eq. (3) blind the La to an important wave vector that implanted ^{8}Li sees, reducing its T_1 and $\mathscr{K}$. The most obvious candidate is the reported AF ordering vector in LNO/LAO superlattices, $\vec{q}_{\rm AF} = (1/4, 1/4, 1/4)$ [42]. However, for the La site $A(\vec{q}_{\rm AF})$ is nonzero, ruling out at least the most obvious explanation along these lines. A second possibility is that (unlike Li), La may have a substantial orbital shift which cannot easily be separated from the temperature-independent Knight shift. Using the full ^{139}La shift may thus result in a significantly overestimated $\mathscr{K}$.

While it is widely accepted that LNO remains a metal to low temperature, the occurrence of static antiferromagnetism (AF) was recently suggested from new data in a single crystal at $T_N \approx 157$ K [16]. In contrast, we have no evidence of magnetic ordering at this temperature, either from the resonance line or $1/T_1$, in agreement with recent data suggesting that the AF is due to an oxygen-deficient phase [17,18].

We turn now to the sample-dependent deviation from the Korringa dependence of $1/T_1$ above 200 K. This bifurcation coincides with a small change in the Ni-O-Ni angle from structural studies on powders [12]. Above about 300 K, $\chi(T)$ for LNO crystals is well described by the phenomenological Curie-Weiss dependence, $\chi \propto (T + \theta)^{-1}$ with a large $\theta \approx 2000$ K, indicating a substantial departure from a simple T-independent Pauli susceptibility. It is interesting that the Korringa dependence in Fig. 2 (the NMR hallmark of a metal) appears to break down close to the onset of this high-T decrease in χ. From analysis of the RF conductivity [11], it was concluded that the carrier density decreases substantially above 200 K which would simultaneously diminish both Korringa slopes. The sample dependence is clearly more complex (Fig. 2). It is also not as simple as an additional relaxation, due to differing impurity content, for example. Rather, it has the opposite sense for the fast and slow components. This suggests the magnetic response depends on subtle details of the temperature evolution of the lattice which are in turn influenced by the epitaxial relation to the substrate.

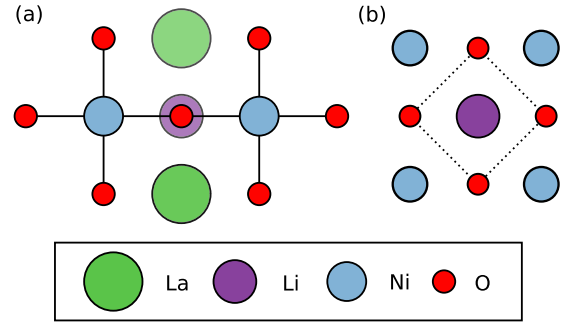

FIG. 5. Schematic of the interstitial $^8Li^+$ site P in perovskite oxides. For simplicity, the illustrated structure is cubic; however, the site retains the same coordination when the symmetry is lowered. (a) Side view illustrating that the Li site is halfway between two neighboring La. (b) Top view of the NiO_2 plane showing that the Li site is coordinated with 4 oxygen anions.

The above features are consistent with a correlated metal lacking static magnetism. However, an essential feature of our data is the two-component character of the relaxation indicating two metallic local environments for ^{8}Li. Phase separation (chemical, crystallographic, or electronic) would be unlikely to result in such a clear separation into two equally abundant signals in the two very different samples. Instead, ^{8}Li probably occupies two distinct crystallographic sites. For example, in simple fcc metals such as Ag and Au [23,39,43], there are two inequivalent cubic sites (distinguished by their hyperfine coupling to the conduction band) and a T-dependent site change transition around 180 K [43]. However, in other perovskite oxides [35–37], we find a single interstitial site characterized by a large quadrupole splitting [35,36,38], which we shall call the P site, at the 3c Wyckoff position in the cubic ($Pm\bar{3}m$) phase. As illustrated in Fig. 5, P is midway between two adjacent A-site (La^{3+}) ions at the center of a square Ni-O plaquette. In contrast to Au and Ag [23,39,43], the two components in LNO are equal in amplitude at all temperatures, and we find no hint of a site change. Equal population of two distinct lattice sites over such a wide range of T, while possible, seems unlikely.

With no obvious second site, we now consider how site P evolves as the crystal symmetry is lowered from the ideal cubic perovskite structure. In the rhombohedral phase (the nominal LNO structure), adjacent NiO_6 octahedra rotate with an equal angle ∼9° and alternating sign [44]. Despite this, there remains a single P site, consistent with the ^{8}Li spectrum in rhombohedral LAO [38]. In the orthorhombic ($Pnma$) structure, the rotation pattern of the NiO_6 octahedra

differs ($a^-a^-c^+$ instead of $a^-a^-a^-$, in Glazer notation [45]), resulting in three distinct *P*-derived Li sites and two distinct oxygen sites in the enlarged unit cell. With a further lowering of symmetry to monoclinic with the rocksalt alternating superlattice of long and short bond NiO_6 octahedra, i.e., the bond disproportionated structure of insulating $RNiO_3$, *P* further diverges into 4 distinct sites (while there are two Ni and three O sites). Note that in all these structures there is a single La (*A*) site. Since these structures are all pseudocubic, the *P*-derived sites are all very similar, with comparable interstitial space to accommodate the implanted ion but slight differences in distances to the near neighbors and in Li-O-Ni angles that in the cubic phase are exactly 90°. Supercell density functional theory (DFT) calculations (Appendix D) confirm that energetically they are all very similar, so that one would expect a randomly implanted $^8Li^+$ to occupy them with equal probability. While a distribution of similar (but distinct) sites in a lower-symmetry structure constitutes an intrinsic microscopic source of inhomogeneity that could account for the resonance width, among these three structures, we have not found an obvious explanation for two equally abundant ^{8}Li environments (detailed in Appendix E). Based on this, we suggest that the precise low-temperature structure of LNO may be none of these commonly considered possibilities.

Interestingly, our DFT calculations predict that the ground-state symmetry of LNO is rhombohedral $R\bar{3}$, where the $a^-a^-a^-$ rotation pattern of the NiO_6 octahedra coexists with the breathing distortion. A similar observation was made earlier in Ref. [46]. In this structure, there are two *P*-derived sites with energies as close as 20 meV when occupied by Li^+. The distortions giving rise to these structural variants are still subtle and not easily distinguished even with high-resolution diffraction [11,12]. The two-component character of the ^{8}Li relaxation demonstrates that a local probe may provide important structural insight, particularly when there is substantial microscopic inhomogeneity as evident in the resonance width. It will be important to carry out structural refinement of the diffraction data based on the $R\bar{3}$ structure. In addition, other local probes (such as ^{17}O or the very difficult ^{61}Ni [47]) would provide further insight into the local structure and properties of $LaNiO_3$.

V. CONCLUSION

Using ion-implanted ^{8}Li β-NMR, we studied the local electronic properties of $LaNiO_3$. SLR measurements revealed two components with linearly temperature-dependent $1/T_1$ below 200 K, consistent with a Korringa mechanism, providing strong microscopic evidence of a conventional metallic state. The ^{8}Li resonance spectrum comprised a single broad line, implying considerable static inhomogeneity at all temperatures. We find no evidence for either an insulating volume fraction or an antiferromagnetic ordering transition. However, the normalized Korringa product $\mathcal{K} = 0.40(10)$ indicates substantial AF correlations. The two-component SLR implies two ^{8}Li environments, both metallic, a feature common to the two samples. We attribute this to two similar but distinct ^{8}Li sites and not to any form of phase separation. However, this implies the local crystal symmetry must be different from any of the three commonly considered possibilities: The rhombohedral $R\bar{3}c$, the orthorhombic *Pnma*, and the monoclinic $P2_1/n$. Based on DFT calculations, we postulate that the local structure of LNO is instead $R\bar{3}$, where the rhombohedral unit cell is expanded by a breathing distortion of the NiO_6 octahedra. This surprising conclusion is inconsistent with the widespread view that the breathing distortion (bond disproportionation) is causally connected to the metal insulator transition in the rare-earth nickelates.

ACKNOWLEDGMENTS

We thank R. Abasalti, D. J. Arseneau, S. Daviel, B. Hitti, and D. Vyas for technical assistance, and E. Benckiser, J. Chakhalian, Z. Salman, and G. Sawatzky for helpful discussions. This work was supported by NSERC Canada. Work at Argonne (crystal synthesis and characterization) was sponsored by the U.S. Department of Energy, Office of Science, Basic Energy Sciences, Materials Science and Engineering Division. Work at MPI-FKF (thin film synthesis and characterization) was supported by the Deutsche Forschungsgemeinschaft (DFG, German Research Foundation) - Projektnummer 107745057 - TRR 80.

APPENDIX A: BEAM ENERGY AND IMPLANTATION DEPTH

The energy of the $^8Li^+$ beam determines the mean implantation depth of the probe into the sample. The β-NMR spectrometer is located on an isolated high-voltage platform and the ion beam can be decelerated (i.e., the desired implantation depth can be chosen) by varying the bias [22,23]. We modeled the implantation using the SRIM Monte Carlo simulation package [48], and results for the beam energies used here are shown in Fig. 6. For the 38 nm film, the implantation energy was chosen to be 2.9 keV (mean depth 13 nm) to minimize the amount of ^{8}Li in the LSAT substrate. In contrast, no such concerns were warranted for the crystal and the full beam energy 27.9 keV (mean depth 100 nm) was used.

APPENDIX B: DECOMPOSITION OF THE SPIN-LATTICE RELAXATION

Here we present a more detailed view of the analysis of the SLR data. The phenomenological fitting function based on Eq. (1) consists of three exponentials with independent rates whose contributions are illustrated in Fig. 7 at 300 K, where the relaxation is fastest. The background component has the largest relaxation rate but by far the smallest amplitude. In contrast, the slow and fast sample components have equal amplitudes, but rates that differ by a factor of ∼4. Note that though small, the background signal is essential for a good fit. It is comparable in both amplitude and rate to similar signals that are clearly evident in samples with much slower relaxation, such as nonmagnetic insulators, e.g., see Ref. [36]. Table I lists the (temperature-independent) values of the full asymmetry A_0, f_S, and f_f for the two samples, with statistical errors from the global fits.

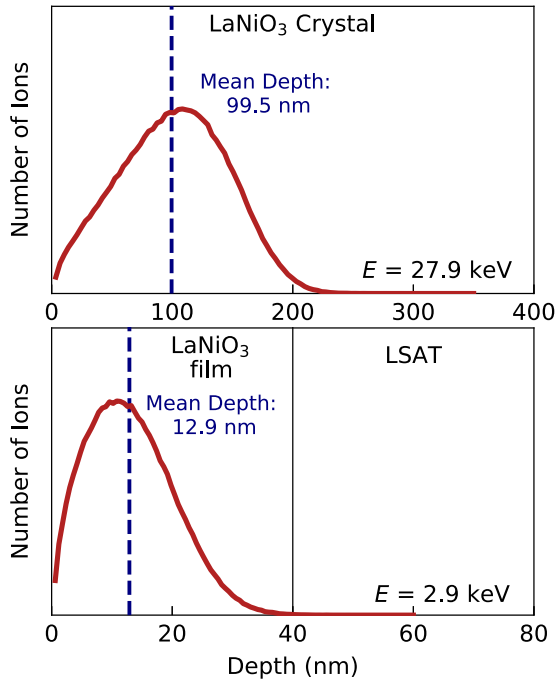

FIG. 6. Stopping distribution of ^{8}Li in a $LaNiO_3$ crystal (top), and a 38 nm film deposited on LSAT (bottom). Obtained using SRIM [48] calculations for implantation energies E of 27.9 keV and 2.9 keV. Each simulation used 10^5 Li ions.

APPENDIX C: DEMAGNETIZATION CORRECTION

The raw shift with respect to MgO is proportional to the static average internal field within the sample. To extract the Knight shift $\mathcal{K}$, it is necessary to account for the contribution from demagnetization [31], which depends on the shape and uniform magnetization of the sample. The crystal is approximately cylindrical, so we use the results of Ref. [49], noting that the demagnetizing field is inhomogeneous in such a non-ellipsoid, and that the sampled volume corresponds to the central region of the face of the crystal to estimate the relevant demagnetization factor $N \approx 0.739$. Using this, we compute the Knight shift $\mathcal{K}$ as

$$\mathcal{K} = K + 4\pi\left(N - \tfrac{1}{3}\right)\chi_0(T), \tag{C1}$$

where $\chi_0(T)$ is the cgs volume susceptibility from Ref. [15]. Figure 8 illustrates the effect of the demagnetization correction by comparing the raw and corrected shifts. In our temperature range, the susceptibility of $LaNiO_3$ is almost constant, making the correction an approximately temperature-independent positive offset of 77(2) ppm. We note that for Li the orbital (chemical) shift $K_{\rm orb}$ is very small, at most 5 ppm [50], and comparable to (or less than) the uncertainty in the measurements. We have, therefore, not attempted to account for it.

TABLE I. The total experimental asymmetry A_0 and the fractions in Eq. (1) from the global fit analysis of the SLR data in LNO.

Sample	A_0	f_S	f_f
Crystal	0.085(3)	0.85(6)	0.50(2)
Film	0.090(3)	0.80(6)	0.50(3)

APPENDIX D: DENSITY FUNCTIONAL CALCULATIONS

Determination of the LNO ground-state symmetry was performed using the projector augmented wave method (PAW) [51,52] as implemented in the Vienna *ab initio* simulation package VASP [53–55]. The generalized gradient approximation (GGA) PBEsol [56] was employed to account for exchange and correlation effects, while a Hubbard-like on-site repulsion U and Hund's exchange coupling J were introduced for the Ni-3d (U = 2.4 or 6 eV and J = 1 eV) and La-4f (U = 14 and J = 1 eV) electrons, following the scheme of Liechtenstein *et al.* [57]. The kinetic energy cutoff was set to 550 eV and a well-converged density of the k-vector mesh, corresponding to $6 \times 6 \times 6$ in a simple cubic perovskite unit cell, was chosen. We compared the total energies of the monoclinic $P2_1/n$ unit cell of LNO and of the rhombohedral $R\bar{3}$ unit cell, both featuring two structurally inequivalent Ni sites but differing in the octahedron's rotation pattern. It is consistently found that the rhombohedral $R\bar{3}$ unit cell has a

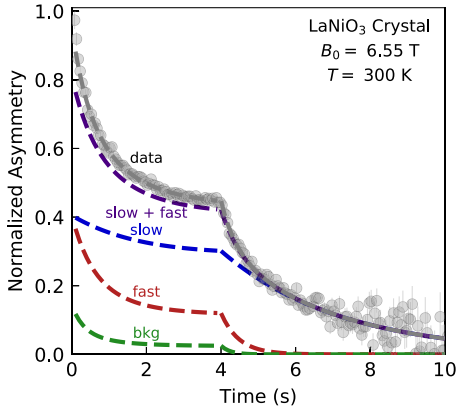

FIG. 7. An example decomposition of the SLR fit to Eq. (1) for the crystal at 300 K and 6.55 T, showing the individual components: Background (green), fast (red), and slow (blue). Also shown: The sum of slow and fast (purple) and the total fit (gray).

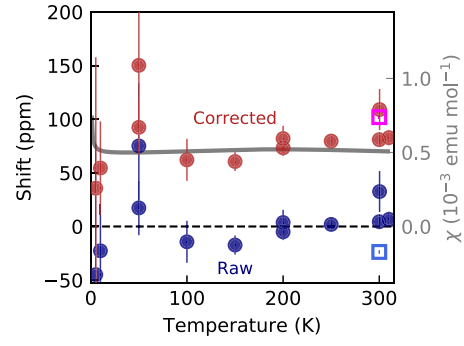

FIG. 8. Comparison of the raw and (demagnetization) corrected shift of the ^{8}Li NMR in the $LaNiO_3$ crystal. The raw shift is obtained by using Eq. (2), while the corrected shift is obtained by applying the demagnetization correction in Eq. (C1). The results at 300 K for the film are shown as open squares. Overlaid on the corrected shifts is the molar susceptibility of the crystal [15], right scale.

lower energy irrespective of the magnetic order imposed [corresponding to either $\vec{q}_{\rm AF} = (1/2, 0, 0)$ or $(1/4, 1/4, 1/4)$ ordering vector] and the U value in the GGA + U scheme chosen ($U = 6$ eV for a robust insulating state and $U = 2.4$ eV for a vanishing charge gap maintaining bond disproportionation). The energy difference between the two structures, however, is only on the order of a few meV per formula unit.

Supercell calculations were performed using both the PAW method via VASP and the linearized augmented plane wave method (LAPW) implemented in the WIEN2K code [58]. For the monoclinic $P2_1/n$ structure we used a $2a \times 2a \times 2a$ supercell, where a is the pseudocubic lattice constant, and imposed the $\vec{q}_{\rm AF} = (1/2, 0, 0)$ antiferromagnetic order onto Ni spins. For the rhombohedral $R\bar{3}$ structure we used a face-centered $4a \times 4a \times 4a$ supercell and imposed the $\vec{q}_{\rm AF} = (1/4, 1/4, 1/4)$ antiferromagnetic order onto Ni spins. A single Li^+ ion was introduced into the various inequivalent P sites (with a compensating uniform background charge) and the system was allowed to fully relax its ionic positions, with the volume fixed to the equilibrium volume of $LaNiO_3$ in PBEsol. The resulting total energies corresponding to different Li^+ positions are found to differ by no more than 140 meV per formula unit in the $P2_1/n$ structure and 20 meV per formula unit in the $R\bar{3}$ structure.

APPENDIX E: DETAILED PROPERTIES OF THE INTERSTITIAL *P* SITE

In an attempt to explain the two ^{8}Li environments, here we present a detailed account of the interstitial P site in the relevant pseudocubic LNO structures. Adopting the approach used successfully in NMR of the cuprates [20], we focus on the hyperfine coupling to the nearest Ni atomic moments. A transferred hyperfine coupling will result from unpaired $3d$ (e_g) orbital spin density being mixed into the mostly vacant Li $2s$ orbital, where it has a Fermi contact coupling to the ^{8}Li nucleus. This mixing can be due to direct overlap, or it can be mediated by the oxygen neighbors. Symmetry considerations, analogous to the Goodenough-Kanamori rules for exchange coupling [59–61], apply to these overlaps, and we expect the coupling to the $d_{x^2-y^2}$ orbital to be zero (both direct and through the oxygen) in the limit of a 90° Li-O-Ni angle. However, for all the pseudocubic distorted structures, the angles are not precisely 90°, so this coupling will be nonzero, but relatively small. The other degenerate e_g orbital, d_{z^2}, should also have a nonzero coupling. This dependence of the hyperfine coupling on angle is clearly demonstrated in the conventional NMR of transition metal oxide Li battery materials [62].

The Knight shift is just proportional to the spin susceptibility, $K = A\chi_s$. Assuming that the macroscopic susceptibility χ is predominantly due to the Ni spins, we estimate the hyperfine coupling A for the slow-relaxing site as $0.78\ {\rm kG}/\mu_B$, a value that is relatively small, e.g., compared to ^{8}Li in simple metals [43] or for substitutional Li in YBCO [63].

In the nominal rhombohedral structure of LNO, the P site has two distinct Li-O-Ni angles of ∼84° and ∼95°, and two distances to the coordinating oxygens. However, all the P sites are equivalent, so this structure is inconsistent with our two component relaxation. Neither of the conventional lower symmetry distorted structures provide a simple doubling of the P site into two equal populations of P-derived sites, but each inequivalent P site will have a different EFG and hyperfine coupling. Although the multiplicity does not match the 1:1 ratio in our data, based on the above considerations, we calculated the distribution of Li-O-Ni angles for all the P-derived sites in both lower symmetry structures (*Pnma* and $P2_1/n$) to see if it clustered approximately into two categories with equal weights. We considered both the ideal structures and ones relaxed around the interstitial Li^+, as estimated by DFT, but we found no indication of an appropriately symmetric bimodal distribution.

The DFT calculations, outlined in Appendix D, find that the ground-state structure is none of the three discussed above, but rather has symmetry $R\bar{3}$. In this structure, the $a^-a^-a^-$ rotation of the NiO_6 octahedra of the rhombohedral unit cell ($R\bar{3}c$) is preserved; however, the symmetry is lowered by bond disproportionation. This results in two Li P sites (and two Ni sites), consistent with our SLR data. However, these two sites must have a different hyperfine coupling to account for the ratio of ∼4 in SLR rates. The distribution of Li-O-Ni angles for both P sites is peaked at 90°, with one much narrower than the other. Given the sensitivity of the hyperfine coupling to angle [64], this structure is a good candidate for explaining the two-component nature of our SLR data.

[1] M. Imada, A. Fujimori, and Y. Tokura, Metal-insulator transitions, Rev. Mod. Phys. **70**, 1039 (1998).

[2] J. B. Torrance, P. Lacorre, A. I. Nazzal, E. J. Ansaldo, and Ch. Niedermayer, Systematic study of insulator-metal transitions in perovskites $RNiO_3$ (R = Pr, Nd, Sm, Eu) due to closing of charge-transfer gap, Phys. Rev. B **45**, 8209 (1992).

[3] M. Greenblatt, Ruddlesden-Popper $Ln_{n+1}Ni_nO_{3n+1}$ nickelates: Structure and properties, Curr. Opin. Solid State Mater. Sci. **2**, 174 (1997).

[4] G. Catalan, Progress in perovskite nickelate research, Phase Transitions **81**, 729 (2008).

[5] S. Catalano, M. Gibert, J. Fowlie, J. Íñiguez, J.-M. Triscone, and J. Kreisel, Rare-earth nickelates $RNiO_3$: Thin films and heterostructures, Rep. Prog. Phys. **81**, 046501 (2018).

[6] V. I. Anisimov, D. Bukhvalov, and T. M. Rice, Electronic structure of possible nickelate analogs to the cuprates, Phys. Rev. B **59**, 7901 (1999).

[7] J. Chaloupka and G. Khaliullin, Orbital Order and Possible Superconductivity in $LaNiO_3/LaMO_3$ Superlattices, Phys. Rev. Lett. **100**, 016404 (2008).

[8] K. Sreedhar, J. M. Honig, M. Darwin, M. McElfresh, P. M. Shand, J. Xu, B. C. Crooker, and J. Spalek, Electronic properties of the metallic perovskite $LaNiO_3$: Correlated behavior of $3d$ electrons, Phys. Rev. B **46**, 6382 (1992).

[9] S. Stemmer and S. J. Allen, Non-Fermi liquids in oxide heterostructures, Rep. Prog. Phys. **81**, 062502 (2018).

[10] J.-S. Zhou, L. G. Marshall, and J. B. Goodenough, Mass enhancement versus Stoner enhancement in strongly correlated

metallic perovskites: $LaNiO_3$ and $LaCuO_3$, Phys. Rev. B **89**, 245138 (2014).

[11] J. Shamblin, M. Heres, H. Zhou, J. Sangoro, M. Lang, J. Neuefeind, J. A. Alonso, and S. Johnston, Experimental evidence for bipolaron condensation as a mechanism for the metal-insulator transition in rare-earth nickelates, Nat. Commun. **9**, 86 (2018).

[12] B. Li, D. Louca, S. Yano, L. G. Marshall, J. Zhou, and J. B. Goodenough, Insulating pockets in metallic $LaNiO_3$, Adv. Electron. Mater. **2**, 1500261 (2015).

[13] J. Chakhalian, J. W. Freeland, A. J. Millis, C. Panagopoulos, and J. M. Rondinelli, Colloquium: Emergent properties in plane view: Strong correlations at oxide interfaces, Rev. Mod. Phys. **86**, 1189 (2014).

[14] A. V. Boris, Y. Matiks, E. Benckiser, A. Frano, P. Popovich, V. Hinkov, P. Wochner, M. Castro-Colin, E. Detemple, V. K. Malik, C. Bernhard, T. Prokscha, A. Suter, Z. Salman, E. Morenzoni, G. Cristiani, H.-U. Habermeier, and B. Keimer, Dimensionality control of electronic phase transitions in nickel-oxide superlattices, Science **332**, 937 (2011).

[15] J. Zhang, H. Zheng, Y. Ren, and J. F. Mitchell, High-pressure floating-zone growth of perovskite nickelate $LaNiO_3$ single crystals, Cryst. Growth Des. **17**, 2730 (2017).

[16] H. Guo, Z. W. Li, L. Zhao, Z. Hu, C. F. Chang, C.-Y. Kuo, W. Schmidt, A. Piovano, T. W. Pi, O. Sobolev, D. I. Khomskii, L. H. Tjeng, and A. C. Komarek, Antiferromagnetic correlations in the metallic strongly correlated transition metal oxide $LaNiO_3$, Nat. Commun. **9**, 43 (2018).

[17] K. Dey, W. Hergett, P. Telang, M. M. Abdel-Hafiez, and R. Klingeler, Magnetic properties of high-pressure optical floating-zone grown $LaNiO_3$ single crystals, J. Cryst. Growth **524**, 125157 (2019).

[18] B.-X. Wang, S. Rosenkranz, X. Rui, J. Zhang, F. Ye, H. Zheng, R. F. Klie, J. F. Mitchell, and D. Phelan, Antiferromagnetic defect structure in $LaNiO_{3-\delta}$ single crystals, Phys. Rev. Mater. **2**, 064404 (2018).

[19] A. Schenck, *Muon Spin Rotation Spectroscopy: Principles and Applications in Solid State Physics* (Adam Hilger, Bristol, 1985).

[20] R. E. Walstedt, Introduction to NMR studies of metals, metallic compounds, and superconductors, *The NMR Probe of High-T_c Materials* (Springer, Berlin, 2008), pp. 13–65.

[21] W. A. MacFarlane, Implanted-ion β-NMR: A new probe for nanoscience, Solid State Nucl. Magn. Reson. **68–69**, 1 (2015).

[22] G. D. Morris, β-NMR, Hyperfine Interact. **225**, 173 (2014).

[23] G. D. Morris, W. A. MacFarlane, K. H. Chow, Z. Salman, D. J. Arseneau, S. Daviel, A. Hatakeyama, S. R. Kreitzman, C. D. P. Levy, R. Poutissou, R. H. Heffner, J. E. Elenewski, L. H. Greene, and R. H. Kiefl, Depth-Controlled β-NMR of ^{8}Li in a Thin Silver Film, Phys. Rev. Lett. **93**, 157601 (2004).

[24] C. D. P. Levy, M. R. Pearson, R. F. Kiefl, E. Mané, G. D. Morris, and A. Voss, Laser polarization facility, Hyperfine Interact. **225**, 165 (2014).

[25] W. A. MacFarlane, T. J. Parolin, D. L. Cortie, K. H. Chow, M. D. Hossain, R. F. Kiefl, C. D. P. Levy, R. M. L. McFadden, G. D. Morris, M. R. Pearson, H. Saadaoui, Z. Salman, Q. Song, and D. Wang, ^{8}Li$^+$ β-NMR in the cubic insulator MgO, J. Phys.: Conf. Ser. **551**, 012033 (2014).

[26] F. James and M. Roos, MINUIT: A system for function minimization and analysis of the parameter errors and correlations, Comput. Phys. Commun. **10**, 343 (1975).

[27] R. Brun and F. Rademakers, ROOT: An object oriented data analysis framework, Nucl. Instrum. Methods Phys. Res., Sect. A **389**, 81 (1997).

[28] T. Moriya, The effect of electron-electron interaction on the nuclear spin relaxation in metals, J. Phys. Soc. Jpn. **18**, 516 (1963).

[29] R. G. Barnes, L. M. Cameron, M. Jerosch-Herold, and C. A. Sholl, Nuclear quadrupolar relaxation in metal-hydrogen systems, J. Alloys Compd. **253–254**, 449 (1997).

[30] W. A. MacFarlane, J. Bobroff, H. Alloul, P. Mendels, N. Blanchard, G. Collin, and J.-F. Marucco, Dynamics of the Local Moment Induced by Nonmagnetic Defects in Cuprates, Phys. Rev. Lett. **85**, 1108 (2000).

[31] M. Xu, M. D. Hossain, H. Saadaoui, T. J. Parolin, K. H. Chow, T. A. Keeler, R. F. Kiefl, G. D. Morris, Z. Salman, Q. Song, D. Wang, and W. A. MacFarlane, Proximal magnetometry in thin films using β-NMR, J. Magn. Reson. **191**, 47 (2008).

[32] S. J. Blundell and S. F. J. Cox, Longitudinal muon spin relaxation in metals and semimetals and the Korringa law, J. Phys.: Condens. Matter **13**, 2163 (2001).

[33] D. L. Cortie, T. Buck, M. H. Dehn, R. F. Kiefl, C. D. P. Levy, R. M. L. McFadden, G. D. Morris, M. R. Pearson, Z. Salman, Y. Maeno, and W. A. MacFarlane, Spin fluctuations in the exotic metallic state of Sr_2RuO_4 studied with β-NMR, Phys. Rev. B **91**, 241113(R) (2015).

[34] A. Sakai, G.-Q. Zheng, and Y. Kitaoka, Strongly correlated metallic state of $LaNiO_3$: ^{139}La NMR study, J. Phys. Soc. Jpn. **71**, 166 (2002).

[35] W. A. MacFarlane, G. D. Morris, K. H. Chow, R. A. Baartman, S. Daviel, K. M. Nichol, R. Poutissou, E. Dumont, L. H. Greene, and R. F. Kiefl, Quadrupolar split ^{8}Liβ-NMR in $SrTiO_3$, Phys. B (Amsterdam) **326**, 209 (2003).

[36] V. L. Karner, R. M. L. McFadden, M. H. Dehn, D. Fujimoto, A. Chatzichristos, G. D. Morris, M. R. Pearson, C. D. P. Levy, A. Reisner, L. H. Tjeng, R. F. Kiefl, and W. A. MacFarlane, Beta-Detected NMR of LSAT and YSZ, JPS Conf. Proc. **21**, 011024 (2018).

[37] V. L. Karner, R. M. L. McFadden, A. Chatzichristos, G. D. Morris, M. R. Pearson, C. D. P. Levy, Z. Salman, D. L. Cortie, R. F. Kiefl, and W. A. MacFarlane, Beta-Detected NMR of $LaAlO_3$, JPS Conf. Proc. **21**, 011023 (2018).

[38] V. L. Karner *et al.*, Quadrupole split ^{8}Li beta NMR in $LaAlO_3$ (unpublished).

[39] M. D. Hossain, H. Saadaoui, T. J. Parolin, Q. Song, D. Wang, M. Smadella, K. H. Chow, M. Egilmez, I. Fan, R. F. Kiefl, S. R. Kreitzman, C. D. P. Levy, G. D. Morris, M. R. Pearson, Z. Salman, and W. A. MacFarlane, The spin lattice relaxation of ^{8}Li in simple metals, Phys. B (Amsterdam) **404**, 914 (2009).

[40] K. Ueda and T. Moriya, Nuclear magnetic relaxation in weakly antiferromagnetic metals, J. Phys. Soc. Jpn. **38**, 32 (1975).

[41] J. L. García-Muñoz, P. Lacorre, and R. Cywinski, Muon-spin-relaxation study of magnetic order in RNiO$_3$ (R = rare earth) below the metal-insulator transition, Phys. Rev. B **51**, 15197 (1995).

[42] A. Frano, E. Schierle, M. W. Haverkort, Y. Lu, M. Wu, S. Blanco-Canosa, U. Nwankwo, A. V. Boris, P. Wochner,

G. Cristiani, H. U. Habermeier, G. Logvenov, V. Hinkov, E. Benckiser, E. Weschke, and B. Keimer, Orbital Control of Noncollinear Magnetic Order in Nickel Oxide Heterostructures, Phys. Rev. Lett. **111**, 106804 (2013).

[43] T. J. Parolin, Z. Salman, K. H. Chow, Q. Song, J. Valiani, H. Saadaoui, A. O'Halloran, M. D. Hossain, T. A. Keeler, R. F. Kiefl, S. R. Kreitzman, C. D. P. Levy, R. I. Miller, G. D. Morris, M. R. Pearson, M. Smadella, D. Wang, M. Xu, and W. A. MacFarlane, High-resolution β-NMR study of $^{8}Li^{+}$ implanted in gold, Phys. Rev. B **77**, 214107 (2008).

[44] G. Gou, I. Grinberg, A. M. Rappe, and J. M. Rondinelli, Lattice normal modes and electronic properties of the correlated metal $LaNiO_3$, Phys. Rev. B **84**, 144101 (2011).

[45] A. M. Glazer, The classification of tilted octahedra in perovskites, Acta Crystallogr., Sect. B **28**, 3384 (1972).

[46] A. Subedi, Breathing distortions in the metallic, antiferromagnetic phase of $LaNiO_3$, SciPost Phys. **5**, 20 (2018).

[47] J. J. van der Klink and H. B. Brom, Relation between susceptibility and Knight shift in $La_2NiO_{4.17}$ and K_2NiF_4 by ^{61}Ni NMR, Phys. Rev. B **81**, 094419 (2010).

[48] J. F. Ziegler, M. D. Ziegler, and J. P. Biersack, SRIM: The stopping and range of ions in matter, Nucl. Instrum. Methods Phys. Res., Sect. B **268**, 1818 (2010).

[49] R. I. Joseph and E. Schlömann, Demagnetizing field in nonellipsoidal bodies, J. Appl. Phys. **36**, 1579 (1965).

[50] J. P. Kartha, D. P. Tunstall, and J. T. S. Irvine, An NMR Investigation of Lithium Occupancy of Different Sites in the Oxide Superconductor $LiTi_2O_4$ and Related Compounds, J. Solid State Chem. **152**, 397 (2000).

[51] P. E. Blöchl, Projector augmented-wave method, Phys. Rev. B **50**, 17953 (1994).

[52] G. Kresse and D. Joubert, From ultrasoft pseudopotentials to the projector augmented-wave method, Phys. Rev. B **59**, 1758 (1999).

[53] G. Kresse and J. Furthmüller, Efficiency of *ab initio* total energy calculations for metals and semiconductors using a plane-wave basis set, Comput. Mater. Sci. **6**, 15 (1996).

[54] G. Kresse and J. Furthmüller, Efficient iterative schemes for *ab initio* total-energy calculations using a plane-wave basis set, Phys. Rev. B **54**, 11169 (1996).

[55] J. Paier, R. Hirschl, M. Marsman, and G. Kresse, The Perdew-Burke-Ernzerhof exchange-correlation functional applied to the G2-1 test set using a plane-wave basis set, J. Chem. Phys. **122**, 234102 (2005).

[56] J. P. Perdew, A. Ruzsinszky, G. I. Csonka, O. A. Vydrov, G. E. Scuseria, L. A. Constantin, X. Zhou, and K. Burke, Restoring the Density-Gradient Expansion for Exchange in Solids and Surfaces, Phys. Rev. Lett. **100**, 136406 (2008).

[57] A. I. Liechtenstein, V. I. Anisimov, and J. Zaanen, Density-functional theory and strong interactions: Orbital ordering in Mott-Hubbard insulators, Phys. Rev. B **52**, R5467(R) (1995).

[58] P. Blaha, K. Schwarz, G. K. H. Madsen, D. Kvasnicka, and J. Luitz, *WIEN2K, An Augmented Plane Wave + Local Orbitals Program for Calculating Crystal Properties* (Karlheinz Schwarz, Technische Universität Wien, Austria, 2001).

[59] J. B. Goodenough, Theory of the role of covalence in the perovskite-type manganites [La, M(II)]MnO_3, Phys. Rev. **100**, 564 (1955).

[60] J. B. Goodenough, An interpretation of the magnetic properties of the perovskite-type mixed crystals $La_{1-x}Sr_xCoO_{3-\lambda}$, J. Phys. Chem. Solids **6**, 287 (1958).

[61] J. Kanamori, Superexchange interaction and symmetry properties of electron orbitals, J. Phys. Chem. Solids **10**, 87 (1959).

[62] C. P. Grey and N. Dupré, NMR studies of cathode materials for lithium-ion rechargeable batteries, Chem. Rev. **104**, 4493 (2004).

[63] J. Bobroff, W. A. MacFarlane, H. Alloul, P. Mendels, N. Blanchard, G. Collin, and J.-F. Marucco, Spinless Impurities in High-T_c Cuprates: Kondo-Like Behavior, Phys. Rev. Lett. **83**, 4381 (1999).

[64] C. Pan, Y. J. Lee, B. Ammundsen, and C. P. Grey, ^{6}Li MAS NMR studies of the local structure and electrochemical properties of Cr-doped lithium manganese and lithium cobalt oxide cathode materials for lithium-ion batteries, Chem. Mater. **14**, 2289 (2002).

Correction: The 18th author's first name contained a misspelling and has been corrected.